JOURNAL OF COMPUTATIONAL PHYSICS 119, 325–341 (1995)

Multigrid Mapping and Box Relaxation for Simulation of the Whole Process of Flow Transition in 3D Boundary Layers*

CHAOQUN LIU AND ZHINING LIU

Center for Computational Mathematics, University of Colorado at Denver, Denver, Colorado 80217-3364

Received February 22, 1994

A new multilevel methodology is developed in this study to provide a successful numerical simulation for the whole process of flow transition in 3D flat plate boundary layers, including linear growth, secondary instability, breakdown, and transition on a relatively coarse grid with low CPU cost. For high-order accuracy, good stability, and fast convergence, this approach uses a fourth-order finite difference scheme on stretched and staggered grids, a fully implicit time-marching technique, a semi-coarsening multigrid based on the so-called approximate line-box relaxation, and a buffer domain for the outflow boundary conditions. A new fine–coarse–fine grid dissipation technique was developed to capture the large eddies and represent the main roles of small eddies to keep the code running after the laminar flow breaks down. The computational results are in good agreement with linear stability theory, secondary instability theory, and some experiments. The computation also reproduced the K-type and C-type transitions observed by laboratory experiments. The CPU cost for a typical case is around 2–9 CRAY-YMP hours.

1. INTRODUCTION

Numerical simulation of flow transition plays a very important role in the study of the flow instability, even though it is limited by current computational resources. To date, most numerical studies using direct numerical simulation (DNS) are restricted to the temporal formulation (cf. [1–5]). They can provide better resolution because their computational domain is relatively small, but the results lack physically realistic representation [11]. Although there have been some spatial studies (cf. [6–11]), spatial DNS is still at its early age [12]. First, most such approaches can predict only the early stages of transition (pre-onset simulation) or fully developed turbulent flow at low Reynolds number without a transition process. Second, they tend to require high CPU cost, generally in the range of 100–1000 CRAY-YMP CPU hours. The existing spatial DNS codes usually blow up when the flow enters the breakdown stage, since non-dissipative central differencing cannot provide proper dissipation produced by eddies smaller than the grid size.

The purpose of this study is to develop an efficient and accurate method to simulate the whole process of transition, including linear growth, secondary instability, breakdown, and transition, with relatively coarse grids and low CPU cost. Since it is very difficult to capture all of the scales after the laminar flow breaks down, the aim is to obtain the large eddies only while representing the roles of small vortices by artificial dissipation. The typical grid used here is $16 \times 34 \times 34$ for each T-S wavelength, with a CPU cost in the range of 2–9 CRAY-YMP hours. The computational results show good agreement with linear and secondary instability theory and experiments by Saric *et al.* [17].

* This work was supported by NASA Langley Research Center under Grant NAS1-19312 and by ICOMP/NASA Lewis Research Center under their 93 turbulence modeling program.

2. GOVERNING EQUATIONS IN GENERAL COORDINATES

Considering the general transformation

$$x = x(\xi, \eta, \zeta),$$
$$y = y(\xi, \eta, \zeta),$$
$$z = z(\xi, \eta, \zeta),$$

then the 3D time-dependent incompressible Navier–Stokes equations can be written as

$$\frac{\partial u}{\partial t} + J\left(\frac{\partial Uu}{\partial \xi} + \frac{\partial Vu}{\partial \eta} + \frac{\partial Wu}{\partial \zeta}\right) + \left(\xi_x \frac{\partial}{\partial \xi} + \eta_x \frac{\partial}{\partial \eta} + \zeta_x \frac{\partial}{\partial \zeta}\right) P - \frac{1}{\mathrm{Re}} \Delta_1 u = 0, \quad (1)$$

$$\frac{\partial v}{\partial t} + J\left(\frac{\partial Uv}{\partial \xi} + \frac{\partial Vv}{\partial \eta} + \frac{\partial Wv}{\partial \zeta}\right) + \left(\xi_y \frac{\partial}{\partial \xi} + \eta_y \frac{\partial}{\partial \eta} + \zeta_y \frac{\partial}{\partial \zeta}\right) P - \frac{1}{\mathrm{Re}} \Delta_1 v = 0, \quad (2)$$

$$\frac{\partial w}{\partial t} + J\left(\frac{\partial Uw}{\partial \xi} + \frac{\partial Vw}{\partial \eta} + \frac{\partial Ww}{\partial \zeta}\right) + \left(\xi_z \frac{\partial}{\partial \xi} + \eta_z \frac{\partial}{\partial \eta} + \zeta_z \frac{\partial}{\partial \zeta}\right) P - \frac{1}{\mathrm{Re}} \Delta_1 w = 0, \quad (3)$$

0021-9991/95 $12.00

$$\frac{\partial U}{\partial \xi}+\frac{\partial V}{\partial \eta}+\frac{\partial W}{\partial \zeta}=0, \tag{4}$$

and

$$U=\frac{1}{J}(u\xi_x+v\xi_y+w\xi_z), \tag{5}$$

$$V=\frac{1}{J}(u\eta_x+v\eta_y+w\eta_z), \tag{6}$$

$$W=\frac{1}{J}(u\zeta_x+v\zeta_y+w\zeta_z), \tag{7}$$

where u, v, w are velocity components; U, V, W are contravariant velocity components; P is pressure; Re is the Reynolds number based on the free stream velocity U_∞, the viscosity parameter ν, and some reference length, for example (δ_0^* is the displacement thickness of boundary layer at inflow),

$$\mathrm{Re}=\frac{U_\infty \delta_0^*}{\nu};$$

J is the transformation Jacobian,

$$J=\frac{\partial(\xi,\eta,\zeta)}{\partial(x,y,z)}=\begin{vmatrix}\xi_x & \xi_y & \xi_z\\ \eta_x & \eta_y & \eta_z\\ \zeta_x & \zeta_y & \zeta_z\end{vmatrix};$$

and Δ_1 is the physical Laplacian operator transformed to the computational (ξ, η, ζ) space:

$$\begin{aligned}\Delta_1=&(\xi_x^2+\xi_y^2+\xi_z^2)\frac{\partial^2}{\partial\xi^2}+(\eta_x^2+\eta_y^2+\eta_z^2)\frac{\partial^2}{\partial\eta^2}\\&+(\zeta_x^2+\zeta_y^2+\zeta_z^2)\frac{\partial^2}{\partial\zeta^2}+2(\xi_x\eta_x+\xi_y\eta_y+\xi_z\eta_z)\frac{\partial^2}{\partial\xi\partial\eta}\\&+2(\xi_x\zeta_x+\xi_y\zeta_y+\xi_z\zeta_z)\frac{\partial^2}{\partial\xi\partial\zeta}\\&+2(\eta_x\zeta_x+\eta_y\zeta_y+\eta_z\zeta_z)\frac{\partial^2}{\partial\eta\partial\zeta}\\&+(\xi_{xx}+\xi_{yy}+\xi_{zz})\frac{\partial}{\partial\xi}+(\eta_{xx}+\eta_{yy}+\eta_{zz})\frac{\partial}{\partial\eta}\\&+(\zeta_{xx}+\zeta_{yy}+\zeta_{zz})\frac{\partial}{\partial\zeta}.\end{aligned} \tag{8}$$

This constitutes seven equations for the seven unknowns u, v, w, U, V, W, and P.

The perturbation equations are obtained by decomposing the total flow into a steady base flow and a perturbation. Using subscript 0 to denote the base flow variables, let

$$\begin{aligned}\mathbf{u}(x,y,z,t)&\leftarrow\mathbf{u}_0(x,y,z)+\mathbf{u}(x,y,z,t),\\ \mathbf{U}(x,y,z,t)&\leftarrow\mathbf{U}_0(x,y,z)+\mathbf{U}(x,y,z,t),\\ P(x,y,z,t)&\leftarrow P_0(x,y,z)+P(x,y,z,t),\end{aligned} \tag{9}$$

where $\mathbf{u}=(u, y, w)$, $\mathbf{U}=(U, V, W)$. Noting that the base flow itself also satisfies the Navier–Stokes equations, we then obtain the governing system for the perturbations:

$$\begin{aligned}\frac{\partial u}{\partial t}+J\Bigg(&\frac{\partial[u(U+U_0)+u_0U]}{\partial\xi}+\frac{\partial[u(V+V_0)+u_0V]}{\partial\eta}\\&+\frac{\partial[u(W+W_0)+u_0W]}{\partial\zeta}\Bigg)+\left(\xi_x\frac{\partial}{\partial\xi}+\eta_x\frac{\partial}{\partial\eta}+\zeta_x\frac{\partial}{\partial\zeta}\right)P\\&-\frac{1}{\mathrm{Re}}\Delta_1 u=0,\end{aligned} \tag{10}$$

$$\begin{aligned}\frac{\partial v}{\partial t}+J\Bigg(&\frac{\partial[v(U+U_0)+v_0U]}{\partial\xi}+\frac{\partial[v(V+V_0)+v_0V]}{\partial\eta}\\&+\frac{\partial[v(W+W_0)+v_0W]}{\partial\zeta}\Bigg)+\left(\xi_y\frac{\partial}{\partial\xi}+\eta_y\frac{\partial}{\partial\eta}+\zeta_y\frac{\partial}{\partial\zeta}\right)P\\&-\frac{1}{\mathrm{Re}}\Delta_1 v=0,\end{aligned} \tag{11}$$

$$\begin{aligned}\frac{\partial w}{\partial t}+J\Bigg(&\frac{\partial[w(U+U_0)+w_0U]}{\partial\xi}+\frac{\partial[w(V+V_0)+w_0V]}{\partial\eta}\\&+\frac{\partial[w(W+W_0)+w_0W]}{\partial\zeta}\Bigg)+\left(\xi_z\frac{\partial}{\partial\xi}+\eta_z\frac{\partial}{\partial\eta}+\zeta_z\frac{\partial}{\partial\zeta}\right)P\\&-\frac{1}{\mathrm{Re}}\Delta_1 w=0,\end{aligned} \tag{12}$$

$$\frac{\partial U}{\partial\xi}+\frac{\partial V}{\partial\eta}+\frac{\partial W}{\partial\zeta}=0. \tag{13}$$

Combined with (5)–(7), this system also has seven equations and seven unknowns for the perturbations.

For the flat plate flow, we use rectangular but stretched grids obtained by a special but relatively simple mapping:

$$\begin{aligned}x&=\xi,\\ y&=y(\eta),\\ z&=\zeta.\end{aligned} \tag{14}$$

This yields

$$\begin{aligned}&J=\eta_y,\\ &\xi_x=\zeta_z=1,\\ &\xi_y=\zeta_z=\eta_x=\eta_z=\zeta_x=\zeta_y=0.\end{aligned} \tag{15}$$

For our numerical simulation, we choose the transformation function

$$y(\eta) = \frac{y_{\max}\sigma\eta}{\eta_{\max}\sigma + y_{\max}(\eta_{\max} - \eta)}, \tag{16}$$

where $y_{\max}$ is the height of the computational domain in the physical coordinate y, $\eta_{\max}$ is the height of the computational domain in the computational coordinate η, and σ is a constant that can be used to adjust the concentration of grid points. This yields the inverse map

$$\eta(y) = \frac{\eta_{\max}y(\sigma + y_{\max})}{y_{\max}(\sigma + y)}. \tag{17}$$

We then obtain

$$\eta_y = \frac{\eta_{\max}\sigma(\sigma + y_{\max})}{y_{\max}(\sigma + y)^2}, \tag{18}$$

$$\eta_{yy} = -\frac{2\eta_{\max}\sigma(\sigma + y_{\max})}{y_{\max}(\sigma + y)^3}. \tag{19}$$

Under the above mapping, the governing equations in the perturbation form can be simplified:

$$\frac{\partial u}{\partial t} + \eta_y\left(\frac{\partial[u(U + U_0) + u_0U]}{\partial\xi} + \frac{\partial[u(V + V_0) + u_0V]}{\partial\eta} + \frac{\partial[uW + u_0W]}{\partial\zeta}\right) + \frac{\partial P}{\partial\xi} - \frac{1}{\mathrm{Re}}\Delta_1 u = 0, \tag{20}$$

$$\frac{\partial v}{\partial t} + \eta_y\left(\frac{\partial[v(U + U_0) + v_0U]}{\partial\xi} + \frac{\partial[v(V + V_0) + v_0V]}{\partial\eta} + \frac{\partial[vW + v_0W]}{\partial\zeta}\right) + \eta_y\frac{\partial P}{\partial\eta} - \frac{1}{\mathrm{Re}}\Delta_1 v = 0, \tag{21}$$

$$\frac{\partial w}{\partial t} + \eta_y\left(\frac{\partial[w(U + U_0) + w_0U]}{\partial\xi} + \frac{\partial[w(V + V_0) + w_0V]}{\partial\eta} + \frac{\partial[wW + w_0W]}{\partial\zeta}\right) + \frac{\partial P}{\partial\zeta} - \frac{1}{\mathrm{Re}}\Delta_1 w = 0, \tag{22}$$

$$\frac{\partial U}{\partial\xi} + \frac{\partial V}{\partial\eta} + \frac{\partial W}{\partial\zeta} = 0, \tag{23}$$

$$U = u/\eta_y, \tag{24}$$

$$W = w/\eta_y, \tag{25}$$

$$V = v. \tag{26}$$

The transformed Laplacian operator in the computational space is simplified as

$$\Delta_1 = \frac{\partial^2}{\partial\xi^2} + \eta_y^2\frac{\partial^2}{\partial\eta^2} + \frac{\partial^2}{\partial\zeta^2} + \eta_{yy}\frac{\partial}{\partial\eta}. \tag{27}$$

In the computational (ξ, η, ζ) space, the grids are uniform. Suppose u, v, w and U, V, W are defined in terms of a staggered grid in the computational space. Here, the values of P are associated with its cell centers, u and U with centers of the cell surfaces parallel to the (η, ζ) plane, v and V with centers of the cell surfaces parallel to the (ξ, ζ) plane, and w and W with centers of the cell surfaces parallel to the (ξ, η) plane.

Second-order backward Euler differences are used in the time direction, and fourth-order central differences are used in space. For the details, see [14].

We can write the discretized governing equations symbolically as follows (Fig. 1):

$$A_{EE}u_{EE} + A_Eu_E + A_Wu_W + A_{WW}u_{WW} + A_{NN}u_{NN} + A_Nu_N + A_Su_S + A_{SS}u_{SS} + A_{FF}u_{FF} + A_Fu_F + A_Bu_B + A_{BB}u_{BB} - A_Cu_C + D_{WW}P_{WW} + D_WP_W + D_EP_E - D_CP_C = S_u, \tag{28}$$

$$B_{EE}v_{EE} + B_Ev_E + B_Wv_W + B_{WW}v_{WW} + B_{NN}v_{NN} + B_Nv_N + B_Sv_S + B_{SS}v_{SS} + B_{FF}v_{FF} + B_Fv_F + B_Bv_B + B_{BB}v_{BB} - B_Cv_C + E_{SS}P_{SS} + E_SP_S + E_NP_N - E_CP_C = S_v, \tag{29}$$

$$C_{EE}w_{EE} + C_Ew_E + C_Ww_W + C_{WW}w_{WW} + C_{NN}w_{NN} + C_Nw_N + C_Sw_S + C_{SS}w_{SS} + C_{FF}w_{FF} + C_Fw_F + C_Bw_B + C_{BB}w_{BB} - C_Cw_C + F_{BB}P_{BB} + F_BP_B + F_FP_F - F_CP_C = S_w, \tag{30}$$

$$DU_{EE}U_{EE} + DU_EU_E + DU_WU_W - DU_CU_C + DV_{NN}V_{NN} + DV_NV_N + DV_SV_S - DV_CV_C + DW_{FF}W_{FF} + DW_FW_F + DW_BW_B - DW_CW_C = S_M, \tag{31}$$

As an illustration of the notation we use, relevant symbols for the discrete ξ-momentum equation are depicted in Fig. 1. The coefficients and source term for the interior points of the discrete ξ-momentum equation (28) associated with u_C are given as

$$A_{EE} = -\frac{1}{12\,\mathrm{Re}\,\Delta\xi^2} + \frac{\eta_{y_C}}{12\Delta\xi}(U_{EE} + 2U_{0_{EE}}),$$

$$A_E = \frac{4}{3\,\mathrm{Re}\,\Delta\xi^2} - \frac{2\eta_{y_C}}{3\Delta\xi}(U_E + 2U_{0_E}),$$

$$A_W = \frac{4}{3\,\mathrm{Re}\,\Delta\xi^2} + \frac{2\eta_{y_C}}{3\Delta\xi}(U_W + 2U_{0_W}),$$

$$A_{WW} = -\frac{1}{12\,\mathrm{Re}\,\Delta\xi^2} - \frac{\eta_{y_C}}{12\Delta\xi}(U_{WW} + 2U_{0_{WW}}),$$

$$A_{NN} = -\frac{\eta_{y_C}^2}{12\,\mathrm{Re}\,\Delta\eta^2} + \frac{\eta_{y_C}}{12\Delta\eta}(V_{nn} + V_{0nn}) - \frac{\eta_{yy_C}}{12\,\mathrm{Re}\,\Delta\eta},$$

$$A_N = \frac{4\eta_{y_C}^2}{3\,\mathrm{Re}\,\Delta\eta^2} - \frac{2\eta_{y_C}}{3\Delta\eta}(V_n + V_{0n}) + \frac{2\eta_{yy_C}}{3\,\mathrm{Re}\,\Delta\eta},$$

$$A_S = \frac{4\eta_{y_C}^2}{3\,\mathrm{Re}\,\Delta\eta^2} + \frac{2\eta_{y_C}}{3\Delta\eta}(V_s + V_{0s}) - \frac{2\eta_{yy_C}}{3\,\mathrm{Re}\,\Delta\eta},$$

$$A_{SS} = -\frac{\eta_{y_C}^2}{12\,\mathrm{Re}\,\Delta\eta^2} - \frac{\eta_{y_C}}{12\Delta\eta}(V_{ss} + V_{0ss}) + \frac{\eta_{yy_C}}{12\,\mathrm{Re}\,\Delta\eta},$$

$$A_{FF} = -\frac{1}{12\,\mathrm{Re}\,\Delta\zeta^2} + \frac{\eta_{y_C}}{12\Delta\zeta}(W_{ff} + W_{0_{ff}}),$$

$$A_F = \frac{4}{3\,\mathrm{Re}\,\Delta\zeta^2} - \frac{2\eta_{y_C}}{3\Delta\zeta}(W_f + W_{0_f}),$$

$$A_B = \frac{4}{3\,\mathrm{Re}\,\Delta\zeta^2} + \frac{2\eta_{y_C}}{3\Delta\zeta}(W_b + W_{0_b}),$$

$$A_{BB} = -\frac{1}{12\,\mathrm{Re}\,\Delta\zeta^2} - \frac{\eta_{y_C}}{12\Delta\zeta}(W_{bb} + W_{0_{bb}}),$$

$$A_C = \frac{3}{2\Delta t} + \frac{5}{2\,\mathrm{Re}}\left(\frac{1}{\Delta\xi^2} + \frac{\eta_{y_C}^2}{\Delta\eta^2} + \frac{1}{\Delta\zeta^2}\right),$$

$$D_E = \frac{1}{24\Delta\xi},$$

$$D_W = D_C = \frac{27}{24\Delta\xi},$$

$$D_{WW} = -\frac{1}{24\Delta\xi},$$

$$S_u = \frac{-4u_C^n + u_C^{n-1}}{2\Delta t} + \eta_{y_C}\left(\frac{-u_{0NN}V_{nn} + 8u_{0N}V_n - 8u_{0S}V_s + u_{0SS}V_{ss}}{12\Delta\eta} + \frac{-u_{0FF}W_{ff} + 8u_{0F}W_f - 8u_{0B}W_b + u_{0BB}W_{bb}}{12\Delta\zeta}\right). \quad (32)$$

Here, superscripts n and $n-1$ are used to indicate values at previous time steps, and superscript $n+1$, which indicates the current time step, is dropped for convenience. Lower case subscripts denote the approximate values of the v and w at points where the associated values of u with capital subscript are located (Fig. 1).

All function values that are required at other than the canonical locations are obtained by fourth-order interpolations in the computational space (see [14]).

The coefficients for the η- and ζ-momentum equations are defined in an analogous way, and the discrete continuity equation is developed simply by applying fourth-order central differences to each term.

3. BOUNDARY CONDITIONS

At the inflow boundary, Benney-Lin type disturbances are imposed:

$$\mathbf{u}(0, y, z, t) = \mathbf{u}_{2d}(y)e^{-i\omega_{2d}t} + \mathbf{u}_{3d}(y)e^{i(-\omega_{3d}t \pm \beta z)}, \quad (33)$$

where ω_{2d} and ω_{3d} are the real frequencies of the disturbance and β is a real constant that represents the spanwise wavenumber.

A no-slip boundary condition is applied at the solid wall. Since the disturbances vanish at infinity, then the boundary conditions at the far field can be specified as

$$\mathbf{u}(x, y \to \infty, z, t) = 0. \quad (34)$$

Actually, we chose $y = y_{\max}$ for the far field, which should be much larger than the displacement thickness. Usually, we use $y_{\max} \geq 50\delta_0^*$, where the disturbance is thought to be negligible.

For flat plate flow, no pressure condition is needed at all the boundaries since a staggered grid is used.

Specification of the outflow boundary conditions is one of the major difficulties in the spatial simulation of flow transition.

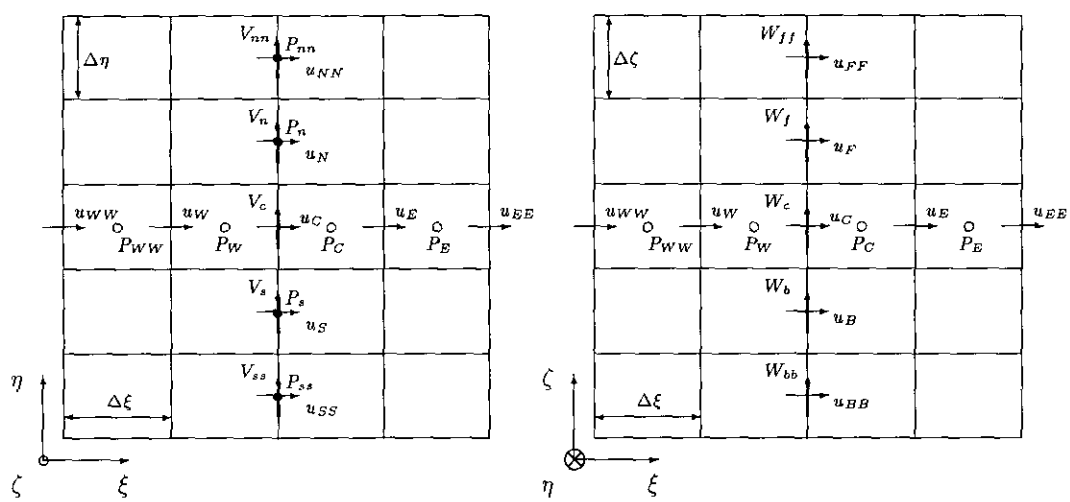

FIG. 1. Neighbor points for ξ-momentum equation (U are at the same points as u and are not shown here).

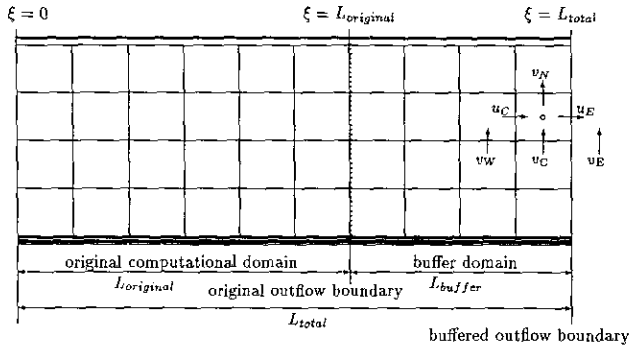

FIG. 2. Extended computational domain.

In [13–15], we developed a very efficient multidomain technique on a staggered grid (see Fig. 2), which eliminates all the visible reflection in a very short buffer domain. For more detail, see [14, 15].

For the flat plate-type flow, the two buffer functions are specified as:

$$b(\xi) = \begin{cases} \tanh\left(\dfrac{L_{\text{total}} - \xi}{L_{\text{buffer}}}\right) \Big/ \tanh(1), & L_{\text{original}} \le \xi \le L_{\text{total}}, \\ 1, & 0 \le \xi \le L_{\text{original}}, \end{cases}$$

$$b_{\text{Re}}(\xi) = \begin{cases} c\dfrac{(\xi - L_{\text{original}})^2}{L_{\text{buffer}}^2} + 1 & L_{\text{original}} \le \xi \le L_{\text{total}}, \\ 1 & 0 \le \xi \le L_{\text{original}}, \end{cases} \tag{35}$$

and (27) is then changed to

$$\Delta_1 = b_{\text{Re}}(\xi)\left\{b(\xi)\frac{\partial^2}{\partial\xi^2} + \eta_y^2\frac{\partial^2}{\partial\eta^2} + \frac{\partial^2}{\partial\zeta^2} + \eta_{yy}\frac{\partial}{\partial\eta}\right\}. \tag{36}$$

Here,

$$c = \max\left\{\frac{\text{Re}}{40} - 1, 1\right\},$$

and the resulting conditions for the buffered outflow boundary are

$$\begin{aligned} U_E &= U_C - \frac{V_N - V_C}{\Delta\eta}\Delta\xi - \frac{W_F - W_C}{\Delta\zeta}\Delta\xi, \\ V_E &= 2V_C - V_W, \\ W_E &= 2W_C - W_W. \end{aligned} \tag{37}$$

4. APPROXIMATE LINE-BOX RELAXATION (ALB)

4.1. *Approximate Box Relaxation (AB)*

The basic idea behind the approximate box relaxation (AB) approach is to schedule relaxation box-by-box, with the same approximate cost as that of Gauss–Seidel relaxation. With a 2D uniform grid (Fig. 3) as an example, we first describe the basic idea of AB.

The generic form of the discrete equations associated with a box for the 2D uniform grids can be written as

$$A_E^C u_E + A_W^C u_W + A_N^C u_N + A_S^C u_S - A_C^C u_C + \frac{P_W - P_C}{\Delta x} = S_{u_C}, \tag{38}$$

$$A_E^E u_{EE} + A_W^E u_C + A_N^E u_{NE} + A_S^E u_{SE} - A_C^E u_E + \frac{P_C - P_E}{\Delta x} = S_{u_E}, \tag{39}$$

$$B_E^C v_E + B_W^C v_W + B_N^C v_N + B_S^C v_S - B_C^C v_C + \frac{P_S - P_C}{\Delta y} = S_{v_C}, \tag{40}$$

$$B_E^N v_{NE} + B_W^N v_{NW} + B_N^N v_{NN} + B_S^N v_C - B_C^N v_N + \frac{P_C - P_N}{\Delta y} = S_{v_N}, \tag{41}$$

$$\frac{u_E - u_C}{\Delta x} + \frac{v_N - v_C}{\Delta y} = 0. \tag{42}$$

Here, the superscripts represent the point at which the discretization is centered. We proceed in the box-by-box process with a few global point Gauss–Seidel relaxation sweeps on the momentum equations, changing u and v and holding P fixed. This means that the four momentum equations (38)–(41) in the box

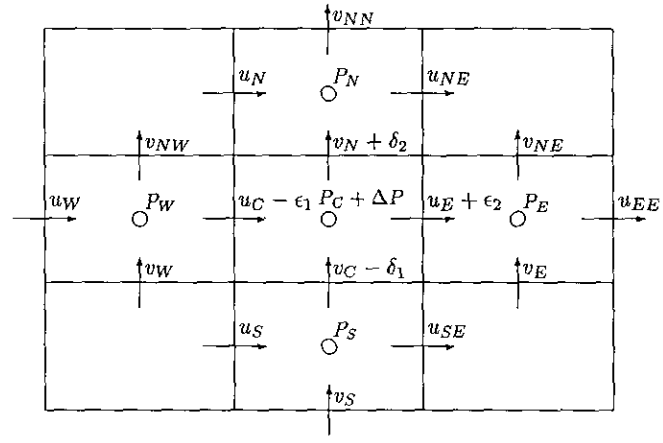

FIG. 3. Approximate box relaxation.

phase are approximately satisfied. Now, proceeding by boxes in some order, we perform distributed relaxation of the form:

$$\begin{aligned} u_C &\leftarrow u_C - \varepsilon_1, \\ u_E &\leftarrow u_E + \varepsilon_2, \\ v_C &\leftarrow v_C - \delta_1, \\ v_N &\leftarrow v_N + \delta_2, \\ P_C &\leftarrow P_C + \Delta P, \end{aligned} \tag{43}$$

where the corrections are chosen to satisfy the discrete continuity equation and four discrete momentum equations associated with the box. Note that the old values of u, v, and P approximately satisfy the associated momentum equations, so we obtain the system for the corrections ε_1, ε_2, δ_1, δ_2, and ΔP,

$$(A_E^C\varepsilon_2 + A_C^C\varepsilon_1) - \frac{\Delta P}{\Delta x} = 0, \tag{44}$$

$$(A_C^E\varepsilon_2 + A_W^E\varepsilon_1) - \frac{\Delta P}{\Delta x} = 0, \tag{45}$$

$$(B_N^C\delta_2 + B_C^C\delta_1) - \frac{\Delta P}{\Delta y} = 0, \tag{46}$$

$$(B_C^N\delta_2 + B_S^N\delta_1) - \frac{\Delta P}{\Delta y} = 0, \tag{47}$$

$$\frac{\varepsilon_1 + \varepsilon_2}{\Delta x} + \frac{\delta_1 + \delta_2}{\Delta y} = S_m, \tag{48}$$

where

$$S_m = -\left(\frac{u_E - u_C}{\Delta x} + \frac{v_N - v_C}{\Delta y}\right).$$

Equations (44) and (45) yield

$$\frac{\varepsilon_1}{\varepsilon_2} = \alpha_0 \equiv \frac{A_C^E - A_E^C}{A_C^C - A_W^E},$$

(46) and (47) yield

$$\frac{\delta_1}{\delta_2} = \beta_0 \equiv \frac{B_C^N - B_N^C}{B_C^C - B_S^N},$$

and together we have

$$\frac{\varepsilon_1}{\delta_1} = \gamma_0 \equiv \frac{B_C^C + B_N^C/\beta_0}{A_C^C + A_E^C/\alpha_0} \cdot \frac{\Delta y}{\Delta x}.$$

Therefore, (48) can be written as

$$\frac{\varepsilon_1 + \varepsilon_1/\alpha_0}{\Delta x} + \frac{\delta_1 + \delta_1/\beta_0}{\Delta y} = S_m, \tag{49}$$

or

$$\frac{\gamma_0(1 + 1/\alpha_0)\delta_1}{\Delta x} + \frac{(1 + 1/\beta_0)\delta_1}{\Delta y} = S_m. \tag{50}$$

The corrections are thus given by

$$\begin{aligned} \delta_1 &= S_m \Big/ \left(\frac{\gamma_0(1 + 1/\alpha_0)}{\Delta x} + \frac{(1 + 1/\beta_0)}{\Delta y}\right), \\ \delta_2 &= \delta_1/\beta_0, \\ \varepsilon_1 &= \delta_1 \cdot \gamma_0, \\ \varepsilon_2 &= \varepsilon_1/\alpha_0, \end{aligned} \tag{51}$$

and

$$\Delta P = (A_C^C\varepsilon_1 + A_E^C\varepsilon_2) \cdot \Delta x.$$

To simplify this scheme, note that, for the case $\Delta t \ll 1$, we have

$$\begin{aligned} &A_C^C \sim A_C^E, \quad B_C^C \sim B_C^N, \\ &A_C^E \gg A_E^C, \quad A_C^C \gg A_W^E, \\ &B_C^N \gg B_N^C, \quad B_C^C \gg B_S^N, \end{aligned}$$

so

$$\begin{aligned} \alpha_0 &\approx 1, \\ \beta_0 &\approx 1, \\ \gamma_0 &\approx \Delta y/\Delta x. \end{aligned}$$

For most cases, we have

$$\begin{aligned} &A_C^E > A_E^C, \quad A_C^C > A_W^E, \\ &B_C^N > B_N^C, \quad B_C^C > B_S^N, \end{aligned}$$

so α_0, β_0, and γ_0 can be approximated in general by

$$\begin{aligned} \alpha_0 &\sim \frac{A_C^E}{A_C^C} \sim 1, \\ \beta_0 &\sim \frac{B_C^N}{B_C^C} \sim 1, \\ \gamma_0 &\sim \frac{B_C^C}{A_C^C} \cdot \frac{\Delta y}{\Delta x}. \end{aligned}$$

For general coordinates, the discrete momentum equations can still be written in the same generic form as that for Cartesian coordinates, but the continuity equation is changed to

$$\frac{U_E - U_C}{\Delta\xi} + \frac{V_N - V_C}{\Delta\eta} = 0. \tag{52}$$

The physical velocities u and v have the following relations with the contravariant velocities U and V:

$$U = au + bv,$$
$$V = cu + dv.$$

This leads the discrete continuity equation to be written as

$$\frac{a_E u_E + b_E \tilde{v}_E - a_C u_C - b_C \tilde{v}_C}{\Delta\xi} + \frac{c_N \tilde{u}_N + d_N v_N - c_C \tilde{u}_C - d_C v_C}{\Delta\eta} = 0,$$

where the superscript $\sim$ represents a point that is not located at a canonical position and therefore requires interpolation. Assuming that

$$(b_E \Delta\tilde{v}_E - b_C \Delta\tilde{v}_C) < (a_E \Delta u_E - a_C \Delta u_C), \tag{53}$$

$$(c_N \Delta\tilde{u}_N - c_C \Delta\tilde{u}_C) < (d_N \Delta v_N - d_C \Delta v_C), \tag{54}$$

then the corresponding correction equation can be approximated by

$$\frac{a_E \varepsilon_2 + a_C \varepsilon_1}{\Delta\xi} + \frac{d_N \delta_2 + d_C \delta_1}{\Delta\eta} = S_m.$$

Note that the defining relations for ε_1, ε_2, δ_1, and δ_2 can be expressed in the same form as for Cartesian coordinates,

$$\frac{\varepsilon_1}{\varepsilon_2} = \alpha_0,$$
$$\frac{\delta_1}{\delta_2} = \beta_0,$$
$$\frac{\varepsilon_1}{\delta_1} = \gamma_0,$$

and

$$\delta_1 = S_m \Big/ \frac{(a_E/\alpha_0 + a_C)\gamma_0}{\Delta\xi} + \frac{(d_N/\beta_0 + d_C)}{\Delta\eta}, \tag{55}$$

where a_E, a_C, d_N, and d_c correspond to the mapping coefficients between u, v and U, V.

4.2. *Approximate line-box relaxation (ALB) for 3D problems*

AB usually works well for 2D problems, but frequently fails to provide fast convergence for 3D problems with anisotropic grids. The basic idea of ALB is to satisfy the continuity equation and momentum equations for all boxes lying on one column simultaneously. Figure 4 gives the distribution of corrections in the (ξ, η) plane for the ALB. This kind of relaxation is very useful when the grids are anisotropic. Assuming, for simplicity, that $\alpha_0 = \beta_0 = 1$, then, according to Fig. 4, ALB solving the discrete system (28)–(31) can be described as follows:

- Freezing P, U, V, W, v, and w, perform line Gauss–Seidel relaxation on (28) over the entire computational domain to obtain a new u.
- Freezing P, U, V, W, u, and w, perform line Gauss–Seidel relaxation on (29) over the entire computational domain to obtain a new v.
- Freezing P, U, V, W, u, and v, perform line Gauss–Seidel relaxation on (30) over the entire computational domain to obtain a new w.
- Use transformation (24)–(26) to obtain new U, V, and W.
- For all $j = 2, 3, \ldots, n_j - 1$ at once: change $U_{i-(1/2)jk}$, $U_{i+(1/2)jk}$, $V_{ij-(1/2)k}$, $W_{ijk-1/2}$, and $W_{ijk+1/2}$ to satisfy the associated continuity equations, then update P_{ijk} so that the new U, V, W, and P, as well as the associated transferred u, v, and w satisfy the three momentum equations.

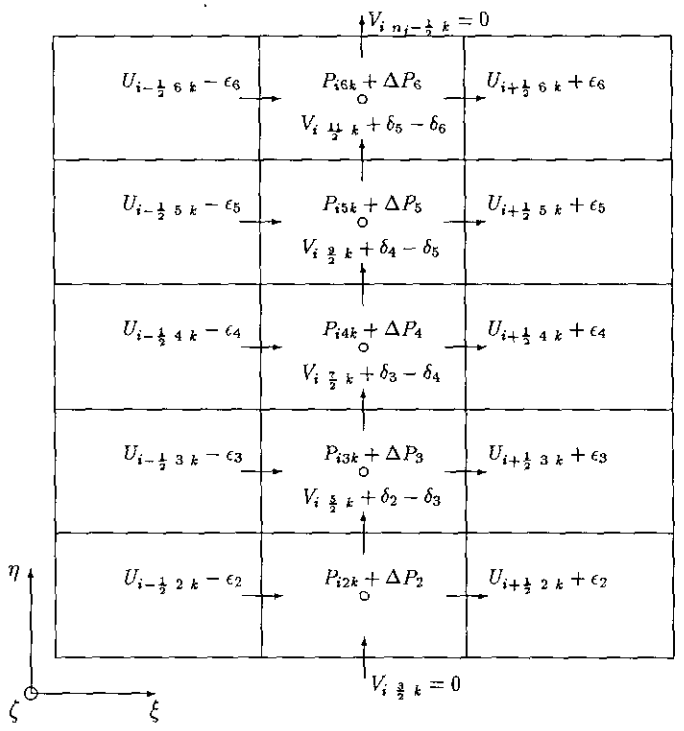

FIG. 4. Distribution of corrections in the (ξ, η) plane.

Since all of the u, v, and w have been previously relaxed, and the U, V, and W are updated, we assume that Eqs. (28)–(30) hold exactly. Let ε, δ, σ, and ΔP represent the corrections for U, V, W, and P, respectively. Thus, for cube ijk (see Fig. 4), the correction equations corresponding to (28)–(31) are

$$(A^{(i-1/2)jk}_{(i+1/2)jk}\,\eta_{y(i+1/2)jk} + A^{(i-1/2)jk}_{(i+1/2)jk}\,\eta_{y(i-1/2)jk})\varepsilon_j - D^{(i-1/2)jk}_{ijk}\,\Delta P_j = 0, \quad (56)$$

$$B^{i(j-1/2)k}_{i(j+1/2)k}(\delta_j - \delta_{j+1}) - B^{i(j-1/2)k}_{i(j-1/2)k}(\delta_{j-1} - \delta_j) - E^{i(j-1/2)k}_{ijk}\,\Delta P_j = 0, \quad (57)$$

$$(C^{ij(k-1/2)}_{ij(k+1/2)}\,\eta_{y_{ijk+1/2}} + C^{ij(k-1/2)}_{ij(k-1/2)}\,\eta_{y_{ijk-1/2}})\sigma_j - F^{ij(k-1/2)}_{ijk}\,\Delta P_j = 0, \quad (58)$$

$$(DU^{ijk}_{(i+1/2)jk} + DU^{ijk}_{(i-1/2)jk})\varepsilon_j + (DW^{ijk}_{ij(k+1/2)} + DW^{ijk}_{ij(k-1/2)})\sigma_j + DV^{ijk}_{i(j+1/2)k}(\delta_j - \delta_{j+1}) - DV^{ijk}_{i(j-1/2)k}(\delta_{j-1} - \delta_j) = S_{m_{ijk}}, \quad j = 2, 3, \ldots, n_j - 1, \quad (59)$$

where the superscripts represent the point at which the discretization is centered. This system has $4(n_j - 2)$ equations for $4(n_j - 2)$ variables. Unfortunately, coupling between the correction variables makes the problem somewhat complicated. To develop a simpler approximate system, define

$$\omega_{xj} = \varepsilon_j/\delta_j,$$
$$\omega_{zj} = \sigma_j/\delta_j.$$

Then Eq. (59) can be written in terms of the unknowns δ_j only:

$$[(DU^{ijk}_{(i+1/2)jk} + DU^{ijk}_{(i-1/2)jk})\omega_{xj} + (DV^{ijk}_{i(j+1/2)k} + DV^{ijk}_{i(j-1/2)k}) + (DW^{ijk}_{ij(k+1/2)} + DW^{ijk}_{ij(k-1/2)})\omega_{zj}]\delta_j - DV^{ijk}_{i(j-1/2)k}\,\delta_{j-1} - DV^{ijk}_{i(j+1/2)k}\delta_{j+1} = S_{m_{ijk}}. \quad (60)$$

Letting

$$a_j = (DU^{ijk}_{(i+1/2)jk} + DU^{ijk}_{(i-1/2)jk})\omega_{xj} + (DV^{ijk}_{i(j+1/2)k} + DV^{ijk}_{i(j-1/2)k}) + (DW^{ijk}_{ij(k+1/2)} + DW^{ijk}_{ij(k-1/2)})\omega_{zj}, \quad (61)$$

$$b_j = -DV^{ijk}_{i(j+1/2)k}, \quad (62)$$

$$c_j = -DV^{ijk}_{i(j-1/2)k}, \quad (63)$$

$j = 2, 3, \ldots, n_j - 1$,

we then obtain the tridiagonal system

$$\begin{bmatrix} a_2 & b_2 & & & & & \\ c_3 & a_3 & b_3 & & & & \\ & \ddots & \ddots & \ddots & & & \\ & & \ddots & \ddots & \ddots & & \\ & & & c_{n_j-2} & a_{n_j-2} & b_{n_j-2} & \\ & & & & c_{n_j-1} & a_{n_j-1} & \end{bmatrix} \begin{bmatrix} \delta_2 \\ \delta_3 \\ \vdots \\ \vdots \\ \delta_{n_j-2} \\ \delta_{n_j-1} \end{bmatrix} = \begin{bmatrix} S_{m_{i2k}} \\ S_{m_{i2k}} \\ \vdots \\ \vdots \\ S_{m_{in_j-2k}} \\ S_{m_{in_j-1k}} \end{bmatrix}. \quad (64)$$

Thus, δ_j, $j = 2, 3, \ldots, n_j - 1$, can be determined very efficiently. The other velocity corrections are given by

$$\varepsilon_j = \omega_{xj}\delta_j,$$
$$\sigma_j = \omega_{zj}\delta_j,$$
$$j = 2, 3, \ldots, n_j - 1.$$

The U, V, and W are then updated on all cells in the i, k η-line as

$$U_{(i+1/2)jk} \leftarrow U_{(i+1/2)jk} + \varepsilon_j,$$
$$U_{(i-1/2)jk} \leftarrow U_{(i-1/2)jk} - \varepsilon_j,$$
$$W_{ij(k+1/2)} \leftarrow W_{ij(k+1/2)} + \sigma_j,$$
$$W_{ij(k-1/2)} \leftarrow W_{ij(k-1/2)} - \sigma_j, \quad (65)$$
$$j = 2, 3, \ldots, n_j - 1,$$
$$V_{i(j-1/2)k} \leftarrow V_{i(j-1/2)k} + \delta_{j-1} - \delta_j, \quad (66)$$
$$j = 3, 4, \ldots, n_j - 1.$$

P is then updated via

$$P_{ijk} \leftarrow P_{ijk} + \Delta P_j, \quad j = 2, 3, \ldots, n_j - 1. \quad (67)$$

Line-box relaxation is efficient when $\Delta z \geq \Delta x$, but degenerates in convergence when $\Delta z \ll \Delta x$. In this case, we need to use alternating line-box relaxation in both y- and z-directions, or plane-box relaxation.

5. SEMI-COARSENING MULTIGRID

For solving the large-scale algebraic systems arising at each time step by the fully implicit scheme for 3D flows, we use a multigrid method based on ALB described in the previous section and a semi-coarsening strategy described below to assure fast convergence. For simplicity of discussion, we consider only the two-grid case.

We use a full approximation scheme (FAS) to accommodate nonlinearities. A two-level FAS algorithm for an equation of the form

$$L^h\phi^h = f^h \tag{68}$$

may be described loosely as

(i) relax on $L^h\phi^h = f^h$,

(ii) solve $L^{2h}\phi^{2h} = L^{2h}I_h^{2h}\phi^h + \tilde{I}_h^{2h}(f^h - L^h\phi^h)$,

(iii) replace $\phi^h \leftarrow \phi^h + I_{2h}^h(\phi^{2h} - I_h^{2h}\phi^h)$.

The notation we have introduced includes the difference operators L^h and L^{2h}, the restriction operators I_h^{2h} (for the approximation) and $\tilde{I}_h^{2h}$ (for the residual), and the interpolation operator I_{2h}^h.

A full-coarsening strategy generally loses efficiency for problems that favor special coordinate directions (e.g., anisotropic problems). To overcome this limitation, we consider now a special combination of semi-coarsening and line-box relaxation. The basic idea is to use line-box relaxation in one direction (say the η-direction) and coarsening only in the other two directions (ξ- and ζ-directions).

Full weighting restriction is again used, but now for transferring the residual from the fine to the semi-coarse grids. The semi-coarsening stencils can be expressed as follows:

$$\tilde{I}_h^{2h}(R_u): \begin{bmatrix} \frac{1}{8} & \frac{1}{4} & \frac{1}{8} \\ \frac{1}{8} & \frac{1}{4} & \frac{1}{8} \end{bmatrix},$$

$$\tilde{I}_h^{2h}(R_v): \begin{bmatrix} \frac{1}{4} & \frac{1}{4} \\ \frac{1}{4} & \frac{1}{4} \end{bmatrix},$$

$$\tilde{I}_h^{2h}(R_w): \begin{bmatrix} \frac{1}{8} & \frac{1}{8} \\ \frac{1}{4} & \frac{1}{4} \\ \frac{1}{8} & \frac{1}{8} \end{bmatrix},$$

$$\tilde{I}_h^{2h}(R_m): \begin{bmatrix} \frac{1}{4} & \frac{1}{4} \\ \frac{1}{4} & \frac{1}{4} \end{bmatrix}. \tag{69}$$

These stencils can be explained geometrically as shown in Fig. 5.

For the restriction of variables, a bilinear-based operator is used. Its stencils are

$$I_h^{2h}(u): \begin{bmatrix} \frac{1}{2} \\ \frac{1}{2} \end{bmatrix}, \quad I_h^{2h}(v): \begin{bmatrix} \frac{1}{4} & \frac{1}{4} \\ \frac{1}{4} & \frac{1}{4} \end{bmatrix},$$

$$I_h^{2h}(w): [\tfrac{1}{2} \quad \tfrac{1}{2}], \quad I_h^{2h}(P): \begin{bmatrix} \frac{1}{4} & \frac{1}{4} \\ \frac{1}{4} & \frac{1}{4} \end{bmatrix}.$$

For semi-coarsening, the coarse to fine transfer operators are based on linear interpolation:

$$I_{2h}^h(\Delta u): \begin{bmatrix} \frac{3}{4} \\ \frac{1}{4} \end{bmatrix} \text{ for } \Delta u_1^h \quad \text{or} \quad \begin{bmatrix} \frac{3}{8} & \frac{3}{8} \\ \frac{1}{8} & \frac{1}{8} \end{bmatrix} \text{ for } \Delta u_2^h,$$

$$I_{2h}^h(\Delta v): \begin{bmatrix} \frac{3}{16} & \frac{9}{16} \\ \frac{1}{16} & \frac{3}{16} \end{bmatrix}, \tag{71}$$

$$I_{2h}^h(\Delta w): [\tfrac{3}{4} \quad \tfrac{1}{4}] \text{ for } \Delta w_1^h \quad \text{or} \quad \begin{bmatrix} \frac{3}{8} & \frac{3}{8} \\ \frac{3}{8} & \frac{1}{8} \end{bmatrix} \text{ for } \Delta w_2^h,$$

$$I_{2h}^h(\Delta P): \begin{bmatrix} \frac{3}{16} & \frac{9}{16} \\ \frac{1}{16} & \frac{3}{16} \end{bmatrix}.$$

The meaning of the above stencils is illustrated in Fig. 6.

6. FINE–COARSE–FINE GRID DISSIPATION

Spatial DNS usually meets difficulties after the flow enters the breakdown stage, where a shear layer develops and the large vortices break down to small-scale vortices. The numerical

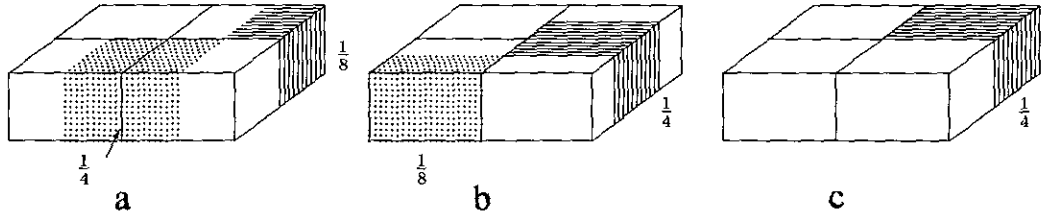

FIG. 5. Full-weighting restriction for (a) ξ-momentum equation, (b) ζ-momentum equation, (c) η-momentum and continuity equations.

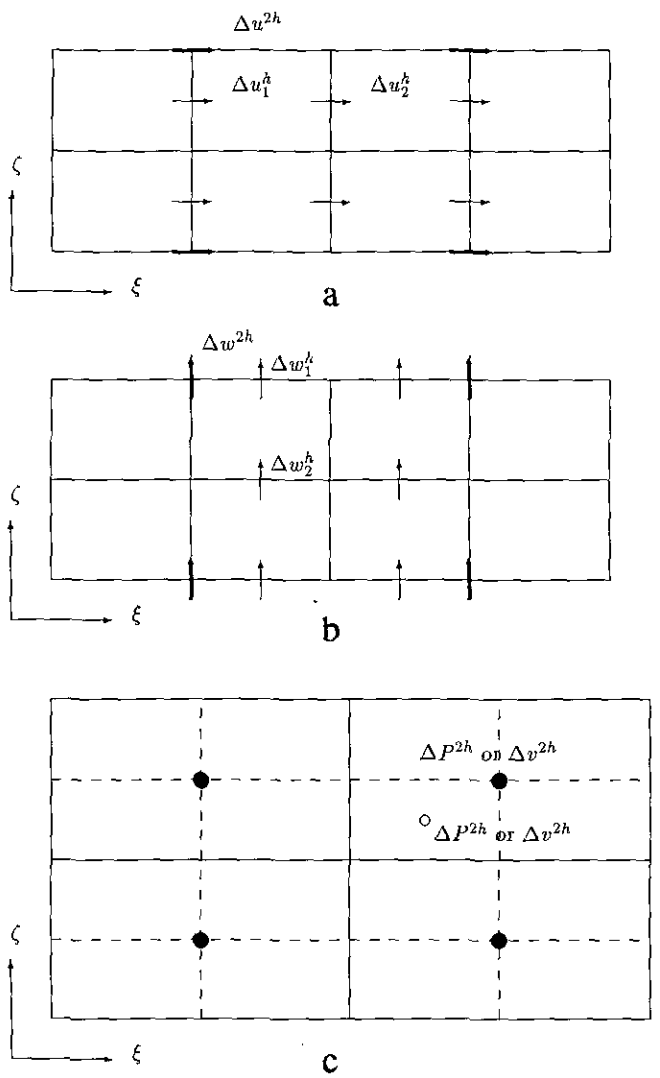

FIG. 6. Bilinear interpolation for (a) Δu, (b) Δw, (c) Δv and ΔP (note that ΔP and Δv are not located in the same (ξ, ζ)-plane).

simulation will thus observe a huge energy burst, the disturbance velocity will be amplified by tens or hundreds of times somewhere inside the flow field, and the code then blows up. Apparently, this is not a physical phenomenon, but largely caused by the lack of dissipation produced by small-scale vortices. To keep the numerical simulation going, we developed a fine–coarse–fine grid dissipation technique. To explain this technique, first consider a 1D problem. We perform fine-to-coarse grid restriction, and then coarse-to-fine grid interpolation at each time step,

$$u_c = I_h^{2h} u_f^{\text{old}},$$

$$u_f^{\text{new}} = I_{2h}^h u_c,$$

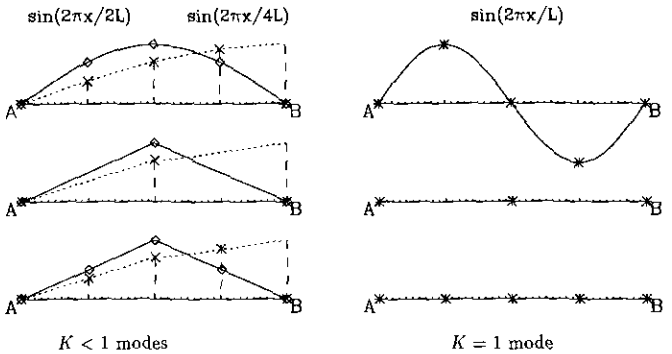

FIG. 7. Fine–coarse–fine grid mapping.

where I_h^{2h} is some linear restriction operator and I_{2h}^h is some linear interpolation operator.

Define $L = \overline{AB}$ as some line segment containing five grid points on the fine grid (see Fig. 7), and (with $u_A \equiv 0$ assumed) define

$$a = \frac{\int_0^L |u_f^{\text{new}}|\, dx}{\int_0^L |u_f^{\text{old}}|\, dx}$$

as the amplification factor of a fine–coarse–fine mapping.

Assume we have different frequency modes, e.g.,

$$\sin\left(K\frac{2\pi}{L}x\right), \quad K = \frac{2}{N-1}, \frac{4}{N-1}, \ldots, 1, \ldots,$$

where

$$L = l \Big/ \left(\frac{N-1}{4}\right),$$

N is the total number of grid points in the entire domain, l is the length of the entire domain, and $K > 1$, which means that there modes are either invisible on, or badly represented by, the coarse grid. We can approximate $a(K)$ by numerical integration for different modes:

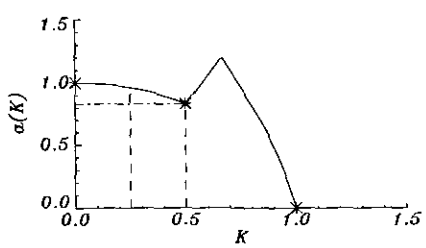

FIG. 8. Amplification factor for different modes.

$$a(K) = \frac{\left[\left|\sin\left(K\frac{2\pi}{L}\frac{L}{2}\right)\right| + \frac{1}{2}\left|\sin\left(K\frac{2\pi}{L}L\right)\right|\right]\frac{L}{2}}{\left[\left|\sin\left(K\frac{2\pi}{L}\frac{L}{4}\right)\right| + \left|\sin\left(K\frac{2\pi}{L}\frac{L}{2}\right)\right| + \left|\sin\left(K\frac{2\pi}{L}\frac{3L}{4}\right)\right| + \frac{1}{2}\left|\sin\left(K\frac{2\pi}{L}L\right)\right|\right]\frac{L}{4}}$$

$$= \frac{2|\sin(K\pi)| + |\sin(2K\pi)|}{\left|\sin\left(\frac{K\pi}{2}\right)\right| + \left|\sin(K\pi)\right| + \left|\sin\left(\frac{3}{2}K\pi\right)\right| + \left|\frac{1}{2}\sin(2K\pi)\right|}.$$

Obviously, $a(1) = 0$, $\lim_{K\to 0} a(K) = 1$.

Figure 8 clearly shows that this kind of grid mapping (fine to coarse restriction and coarse to fine interpolation) significantly damps high-frequency ($K \sim 1$), but has only minor effect on other modes ($K < 1$) and negligible effect on low frequency modes ($K \to 0$).

For certain grids, the highest frequency that can be well simulated is $K = 2(N-2)/(N-1)$. The high-frequency modes may generate higher frequencies, which cannot be simulated by current grids and may cause the computation to fail. This fine–coarse–fine grid dissipation damps the high-frequency modes but protects the low frequency modes. Of course, we do not want to eliminate the high-frequency modes, but we do want to restrict their energy growth.

The actual procedure is given by the steps:

1. $u_c = I_h^{2h} u_f^{\text{old}}$,
2. $u_f^{\text{new}} = (1 - \delta)u_f^{\text{old}} + \delta I_{2h}^h u_c$.

Here, we choose

$$\delta = c \cdot (u^2 + v^2 + w^2),$$

which is proportional to the perturbation kinetic energy with proportionality $c = c(\Delta x, \Delta y, \Delta z, \Delta t)$. Therefore, there is very little damping to high-frequency modes when the perturbation is very small. In this way, we successfully keep the code running to simulate the whole process of transition: linear growth, secondary instability, breakdown, and transition. Note that the large eddies play a much more important role in flow transition than the small eddies that correspond to high frequency modes. We have to sacrifice these small eddies to the limited computer resources. But the physics of transition and turbulence are still simulated quite well because of the accurate representation of lower frequency modes corresponding to the large eddies. This technique actually adds artificial dissipation representing the main roles of small eddies to avoid the huge numerical energy burst. Choice of the dissipation weight δ is somewhat ad hoc,

$$\delta = a\frac{\Delta x \Delta y \Delta z}{\Delta t} \cdot (u^2 + v^2 + w^2),$$

where a is a constant (usually greater than 1). Optimization of δ should improve the performance further.

7. COMPUTATIONAL RESULTS

7.1. *Comparison with Linear Stability Theory (LST)*

To verify the accuracy of our approach, we compare our results with linear theory by assuming a parallel steady base flow and imposing a small disturbance at inflow. The base flow is now $u_0(x, y) = u_0(x_0, y)$, $v_0(x, y) = w_0(x, y) = 0$, where $u_0(x_0, y)$ is the streamwise component of the Blasius similarity solution at inflow, and the wall-normal component has been set to zero to force an artificial parallel base flow.

Let $\text{Re} = \text{Re}_0^* = 900$, $\text{Fr} = 86$ ($\omega = 0.0774$), and $\beta = 0.1$. The Orr–Sommerfeld solution provides an eigenvalue $\alpha = \alpha_R + i\alpha_I = 0.2169 - i0.00419$. In LST, the disturbances are assumed to be traveling waves, for instance, the streamwise velocity can be expressed as

$$u = \varepsilon e^{-\alpha_I x}[\phi_R^u \cos(\alpha_R x + \beta z - \omega_R t) - \phi_I^u \sin(\alpha_R x + \beta z - \omega_R t)], \tag{72}$$

where ε is the amplitude of the perturbation, and ϕ_R and ϕ_I are the respective real and imaginary parts of the eigenfunction obtained from LST.

A $194 \times 50 \times 18$ grid, which includes a five T-S wavelength physical domain and an one T-S wavelength buffer, is used. The amplitude of the perturbation is set to $\varepsilon = 5 \times 10^{-4}$ rms, which is measured as the maximum streamwise disturbance velocity in the wall normal direction during one T-S period, and the stretch parameter is $\sigma = 4.25$. The computational domain is

$$x_0^* \in [303.94, 477.74],$$

$$y_0^* \in [0, 50],$$

$$z_0^* \in [-31.42, 31.42].$$

Semi-coarsening multigrid works well for this case. A 0.2 convergence factor (defined as $\text{Residual}_{\text{new}}/\text{Residual}_{\text{old}}$ is generally observed for each $V(2, 2)$ cycle, which uses two relaxations before and after coarse grid correction on each grid level. The numerical results are then compared with LST. Figure 9a depicts the perturbation amplification factor, $\max\{|u(\text{Re}^*)|\}/\max\{|u(\text{Re}_0^*)|\}$, showing a good agreement with LST, and Fig. 9b gives the contour plots of 2D streamfunction at different time on the plane $k = 9$, showing no visible reflection at either the outflow or the far-field. The profiles of the rms perturbation velocity components at $x^* = 419.8$ are given in Fig. 10, also showing good agreement with LST.

7.2. *Secondary Instability and Transition*

Now suppose that the base flow is not parallel to the solid wall, but that it is, instead, the Blasius similarity solution, which is widely used as the base flow for flat plate transition. A

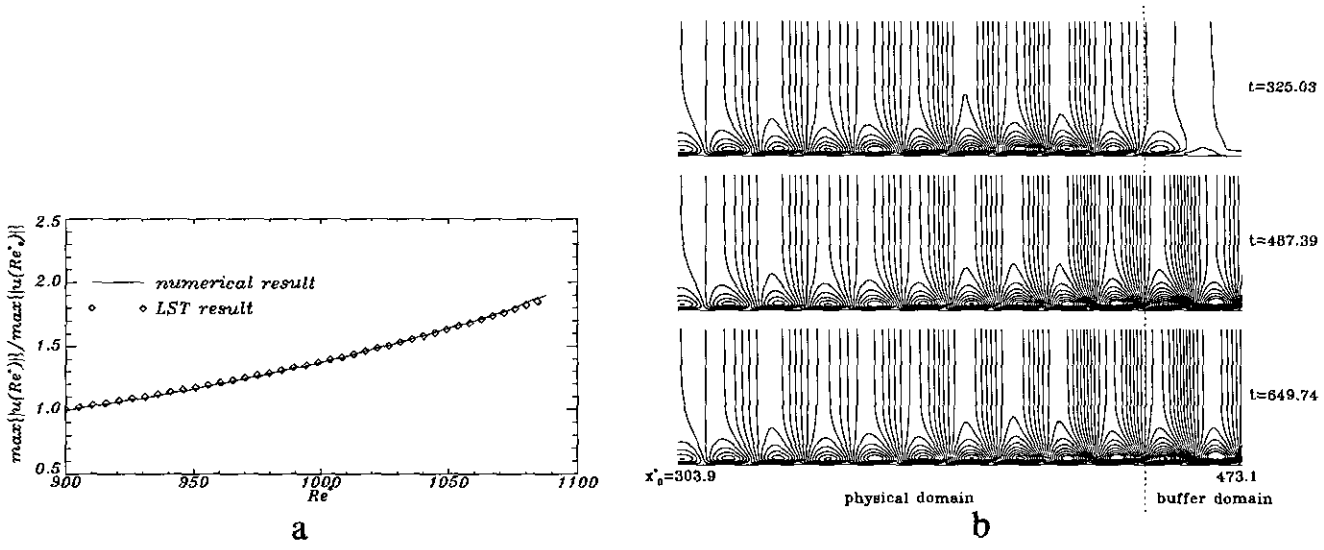

FIG. 9. (a) Comparison of the perturbation amplification rate between numerical results and LST for the small disturbance case. (b) Contour plots of 2D streamfunction at $t = 325.03, 487.39, 649.74$ for the $k = 9$ plane. Contours from -0.006 to 0.006, contour level $= 4.286 \times 10^{-4}$. $\mathrm{Re}_0^* = 900$, $\omega = 0.0774$, $\beta = 0.1$, $\varepsilon_{3d} = 5 \times 10^{-4}$ rms; grids $194 \times 50 \times 18$.

Benney-Lin type disturbance is imposed on the inflow,

$$\mathbf{u}(0, y, z, t) = \mathrm{Real}\{\varepsilon_{2d}\phi_{2d}^{(k)}(y)e^{-i\omega_{2d}t} + \varepsilon_{3d+}\phi_{3d+}^{(k)}(y)e^{-i\omega_{3d}t+i\beta z} + \varepsilon_{3d-}\phi_{3d-}^{(k)}(y)e^{-i\omega_{3d}t-i\beta z}\},$$

where $\phi_{2d}(y)$ and $\phi_{3d\pm}(y)$ correspond respectively to 2D and 3D eignsolutions of the Orr–Sommerfeld equation and the superscript (k) denotes different velocity components. The following is a typical case we chose:

$$\mathrm{Re}_0^* = 900, \quad \mathrm{Fr} = 86\ (\omega_{2d} = \omega_{3d} = 0.0774),$$

$$\beta = 0.1, \quad y_{\max} = 50,$$

$$\alpha_{2d} = 0.2229 - 0.00451i,$$

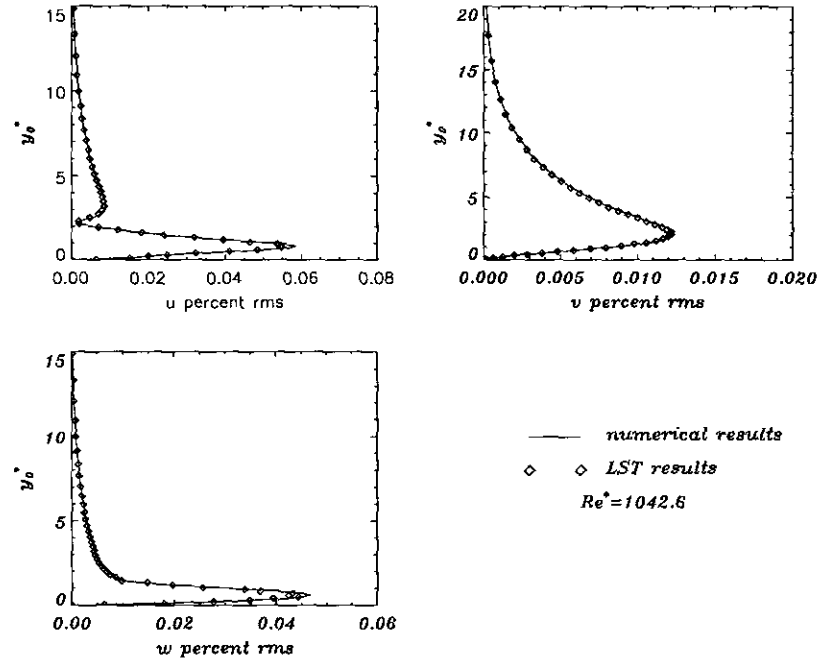

FIG. 10. Comparison of the numerical and LST velocity profiles at $\mathrm{Re}^* = 1042.6$. $\mathrm{Re}_0^* = 900$, $\omega = 0.0774$, $\beta = 0.1$, $\varepsilon_{3d} = 5 \times 10^{-4}$ rms; grids $194 \times 50 \times 18$.

$$\alpha_{3d} = 0.2169 - 0.00419i,$$

$$\varepsilon_{2d} = 0.03, \quad \varepsilon_{3d\pm} = 0.01,$$

$$x_0^* = 303.9, \quad x_{\text{end}}^* = 593.6.$$

The grid we used here is $162 \times 34 \times 34$ (including an 8 T-S wavelength physical domain and a 2 T-S wavelength buffer domain), and the stretch pararmeter is $\sigma = 3.75$. The fully implicit scheme we used in this work has much better stability, which is important for some applications, such as wall suction and blowing. However, for accuracy reasons, we set the time step to $\frac{1}{280}$ of the 3D T-S period.

It took around 9 CRAY-YMP CPU hours for the code to run 30 T-S periods. Figure 11 depicts the contours of the total vorticity magnitude at different times in the plane $y_0^* = 0.1123$, which clearly show the process of λ-wave formation, the peak and valley splitting, and vortex breakdown. It is found that the breakdown begins at the second peak when the λ-wave is

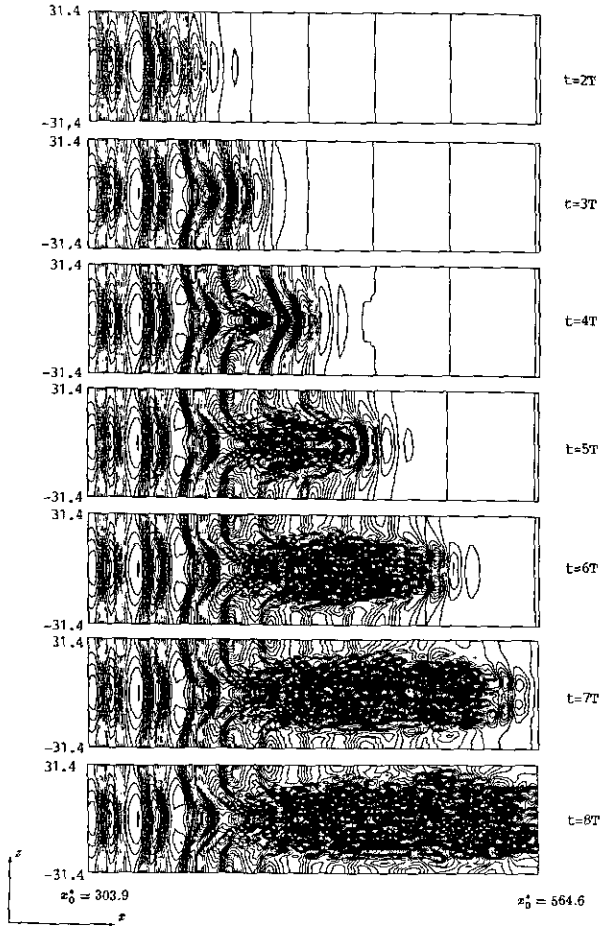

FIG. 11. Contour plots of the total vorticity magnitude obtained on a 162 × 34 × 34 gird at different times on the plane $y_0^* = 0.1123$, Re* = 900, Fr = 86, $\beta = 0.1$, $\varepsilon_{2d} = 0.03$, $\varepsilon_{3d} = 0.01$. Contour interval is 0.02; flow direction is from left to right.

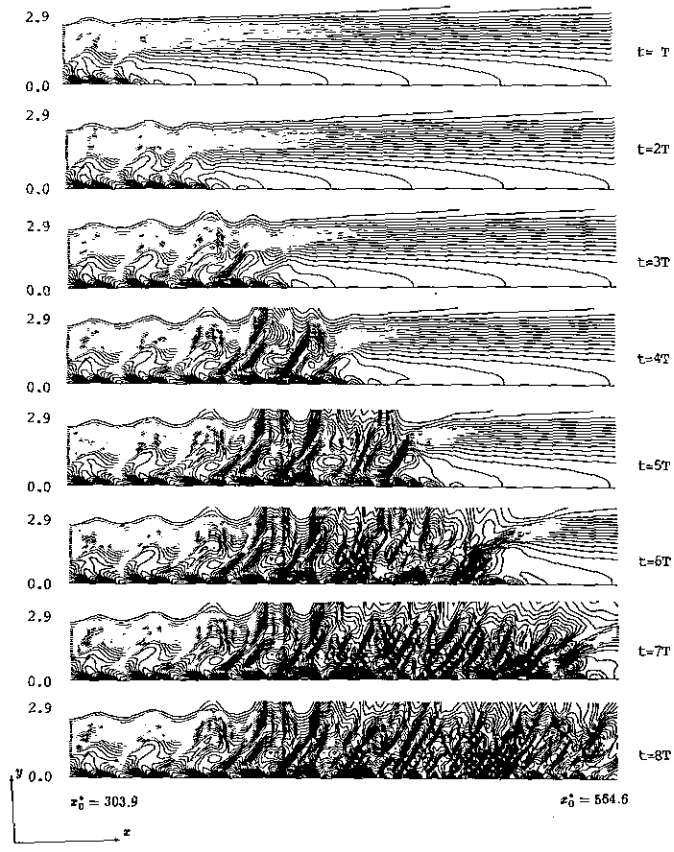

FIG. 12. Contours plots of spanwise vorticity on the plane $z_0^* = 0$ at different times. Re* = 900, Fr = 86, $\beta = 0.1$, $\varepsilon_{2d} = 0.03$, $\varepsilon_{3d} = 0.01$. Contour interval is 0.02; flow direction is from left to right.

intensified to a certain degree and the shear flow develops. Vortex breakdown further contaminates the flow field, leading to a transition process. The patterns of relative helicity (defined as $\mathbf{v} \times \boldsymbol{\Omega}/(|\mathbf{v}| \cdot |\boldsymbol{\Omega}|)$, where $\mathbf{v}$ is the total velocity vector, and $\boldsymbol{\Omega}$ is the vorticity vector) at $t = 30T$ are very similar to those at $t = 7T$, which suggests that the process of transition has been built up after $t = 7T$ in this grid. Less than 2 CRAY-YMP hours were needed to simulate the transition process for a $162 \times 34 \times 34$ grid and seven T-S periods. Figure 12 depicts the spanwise vorticity on the plane $z_0^* = 0$ at different times, which clearly show the process of vortex breakdown and the formation of multiple spikes. The appearance of random moving small vortices after breakdown provides a clue that the flow no longer maintains its laminar status.

We also averaged u and v on the plane $z_0^* = 0$ at different streamwise positions after the transition process was built up. Figure 13 depicts the difference between the $\bar{u}$ profile and the Blasius similarity solution at $x_0^* = 537$, which qualitatively agrees with the experimental results given by Suder, O'Brien, and Reshotko [16]. It also shows that the $\bar{u}$-profile in the transition zone is sharper than those of the Blasius solution, and the wall stress $\tau = \mu(\partial u/\partial y)$ is then larger than that of laminar flow.

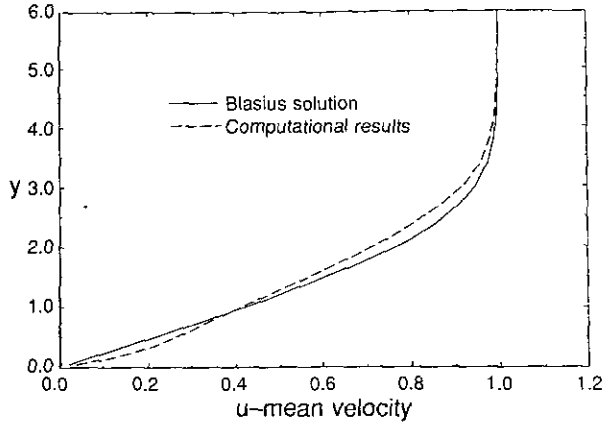

FIG. 13. Comparison between $\bar{u}$-profiles and the Blasius profile at $x_0^* = 537$, $z_0^* = 0$, $\mathrm{Re}_0^* = 900$, Fr = 86, $\beta = 0.1$, $\varepsilon_{2d} = 0.03$, $\varepsilon_{2d} = 0.01$.

Figure 14 gives the $\bar{v}$-profile. $\bar{v}$ is always positive in a laminar boundary layer, but our computational results show that $\bar{v}$ varies from positive to negative and then becomes positive again. This is a typical sign that the flow is experiencing transition.

We also tested another case:

$$\mathrm{Re}_0^* = 732, \quad \beta = 0.2418,$$
$$\omega_{2d} = 0.0909, \quad \omega_{3d} = 0.04545,$$
$$y_{\max} = 75, \quad \sigma = 3.75,$$
$$\alpha_{2d} = 0.2490 - 0.00351i,$$
$$\alpha_{3d} = 0.1103 + 0.00650i,$$
$$\varepsilon_{2d} = 0.015, \quad \varepsilon_{3d\pm} = 0.005,$$
$$x_0 = 248.2, \quad x_{\mathrm{end}} = 437.5.$$

The grid we used here is again 162 × 34 × 34 (including an eight 2D T-S wavelength physical domain and a two 2D T-S

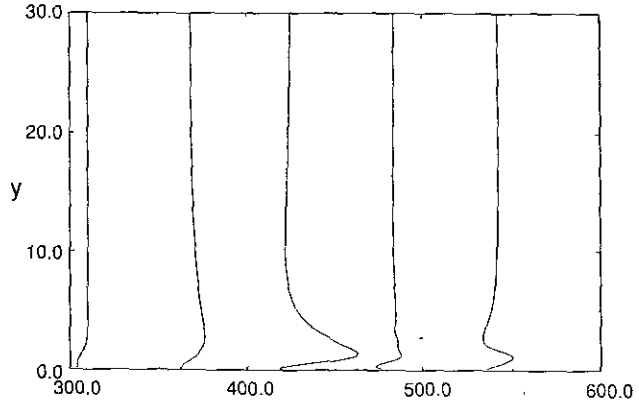

FIG. 14. Time-averaged $\bar{v}$-profiles at $z_0^* = 0$, $x_0^* = 304$, 362, 421, 479, and 537. $\mathrm{Re}_0^* = 900$, Fr = 86, $\beta = 0.1$, $\varepsilon_{2d} = 0.03$, $\varepsilon_{3d} = 0.01$.

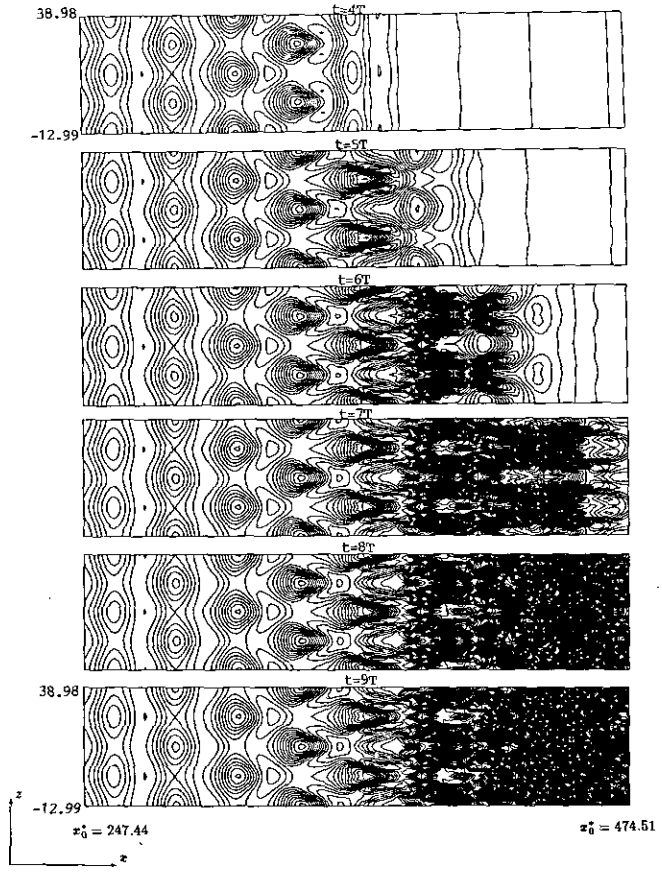

FIG. 15. Contour plots of the total vorticity magnitude of subharmonic transition obtained on a 162 × 34 × 34 gird at different times on the plane $y_0^* = 0.237$. $\mathrm{Re}_0^* = 732$, $\beta = 0.2418$, $\varepsilon_{2d} = 0.015$, $\varepsilon_{3d} = 0.005$. Contour interval is 0.015; flow direction is from left to right.

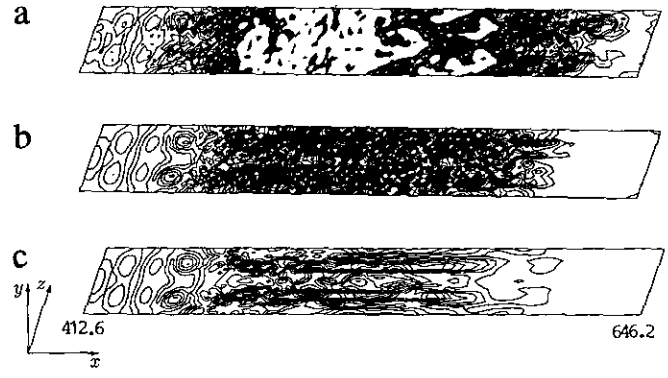

FIG. 16. Contour plots of perturbation vorticity magnitude on the plane $j = 2$ at $t = 406.55$. (a) $a = 0.75$, (b) $a = 2$, (c) $a = 10$. $\mathrm{Re}_0^* = 1221.77$, $\varepsilon_{2d} = 0.01$, $\varepsilon_{3d} = 0.005$, $\Delta t = 0.3078$, grids 162 × 34 × 18 (9 T-S wavelengths physical domain and 1 T-S wavelength buffer).

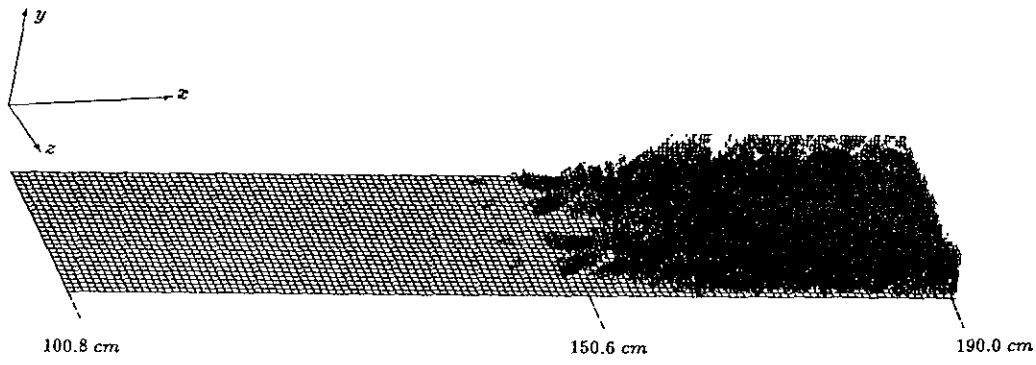

FIG. 17. Three-dimensional contour plots of relative helicity for the fundamental breakdown case.

wavelengths buffer domain) and one 2D T-S period is divided into 150 time steps. Subharmonic transition can be very clearly observed in Fig. 15.

The effect of choosing a different a on the fine–coarse–fine dissipation function is shown on Fig. 16. It is clear that if a is too small, the perturbation may be overamplified and the computation may blow up. In Fig. 16a, we choose $a = 0.75$, and the computation terminated around $t = 7$ T-S periods. However, if a is too large, the perturbation is so seriously smoothed that no laminar flow breakdown or turbulence can be observed. Figure 16c ($a = 10$) depicts this kind of behavior.

Two cases with relatively large computation domains are then employed to simulate the whole process of transition in a flat plate for comparison with experiments by Saric *et al.* [17]. The imposed data is obtained from the experiments by Saric *et al.* [17]. Here, we assume that $U_\infty = 7.5$ m/s and $\nu = 15 \times 10^{-6}\text{m}^2/\text{s}$.

Fundamental Breakdown. The first case is for simulating the fundamental breakdown process. The inflow boundary position is set to $\text{Re}_0^* = 1221.77$, and we let $\omega_{2d} = \omega_{3d} = 0.0928$, $\beta = \alpha_{R_{3d}} = 0.2451$, and $\alpha_{R_{2d}} = 0.2690$. The computational domain is restricted to

$$x_0^* \in [x_0, x_0 + 18\lambda_{2d0}],$$

$$y_0^* \in [0, 50],$$

$$z_0^* \in [-25.635, 76.906],$$

where λ_{2d0} is the 2D T-S wavelength at inflow (the T-S wavelength λ varies when the base flow is non-parallel). The stretch parameter $\sigma = 4.05$. Here $\varepsilon_{2d} = 0.0056$ and $\varepsilon_{3d\pm} = 0.0004$, making the total amplitude of the disturbance at inflow 0.45% rms. The grid we used here is $290 \times 34 \times 30$, and the time step is set to $\frac{1}{220}$ of the 2D T-S wave period. It takes around 9 CRAY-YMP CPU hours for the code to run 20 T-S periods.

Figure 17 depicts the 3D contours of the relative helicity, which shows that the occurrence position of the λ wave is almost the same as that obtained by Saric *et al.* (to compare it with the experiments, all thet labels in the following pictures have been interpreted to those used by Saric *et al.* [17]).

The location of a transition is defined as the position where the sign of $\partial u/\partial x$ at fixed y first changes from negative to positive. At $j = 2$, the above phenomenon occurs at $x_0^* = 646$, which is equivalent to $x = 1.579\ m$ in the laboratory experiment, or $\text{Re}_\delta = \sqrt{\text{Re}_x} = 868$. The normalized maximum perturbation velocity amplitude as a function of Re_δ is given in Fig. 18, showing good agreement with the experiments.

Subharmonic Breakdown. The second case is subharmonic breakdown. The inflow position is still the same as fundamental breakdown, but the parameters are changed according to the experiment:

$$\text{Re}_0^* = 1221.77, \quad \beta = 0.178,$$

$$\omega_{2d} = 0.0928, \quad \omega_{3d} = 0.0464,$$

$$\alpha_{2d} = 0.268986 - 0.00871657i,$$

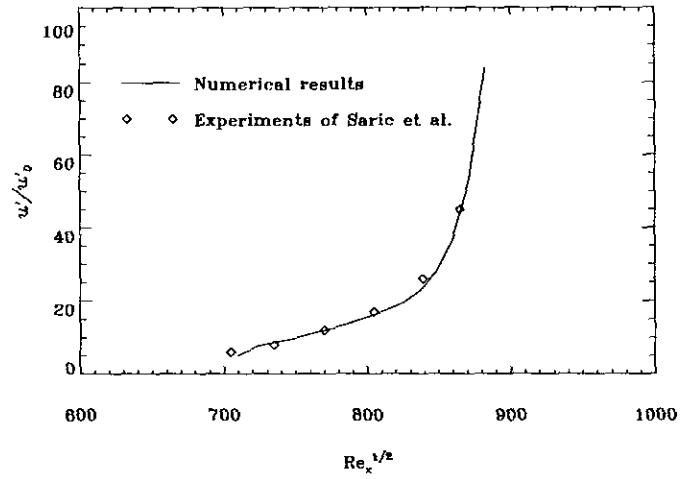

FIG. 18. Amplitude as a function of Re_δ with experimental results of Saric *et al.* [17].

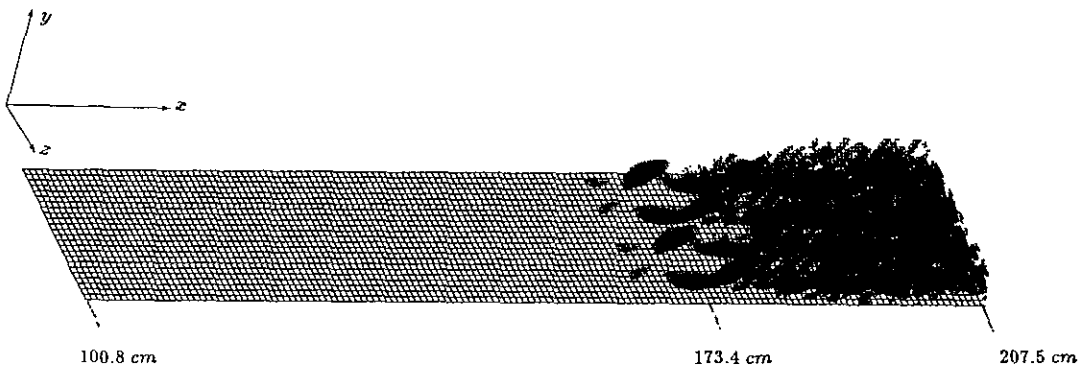

FIG. 19. Three-dimensional contour plots of relative helicity for the subharmonic breakdown case.

$$\alpha_{3d} = 0.12965 - 7.831 \times 10^{-4} i,$$

$$\varepsilon_{2d} = 0.0030, \quad \varepsilon_{3d} = 0.000125.$$

The computational domain is then changed to

$$x_0^* \in [x_0, x_0 + 21\lambda_{2d0}],$$

$$y_0^* \in [0, 50],$$

$$z_0^* \in [-35.3, 105.9],$$

and the stretch parameter $\sigma = 4.15$.

We use a $338 \times 34 \times 26$ grid, which includes a twenty 2D T-S wavelength physical domain and an one 2D T-S wavelength buffer. Ten CRAY CPU hours are required to run twenty 2D T-S periods. Figure 19 depicts the 3D contours of relative helicity at $t = 20T$, showing clearly the staggered structure of the λ waves. The transition location measured at $j = 2$ and $k = 13$ is $x_0^* = 756$, which converts to $x = 1.847$ m or $\mathrm{Re}_\delta = 961$. Figure 20 gives the comparison of normalized amplitude of perturbation velocity as a function of Re_δ, obtained at $u = 0.4$, also showing good agreement with the experiment by Saric *et al.* [17].

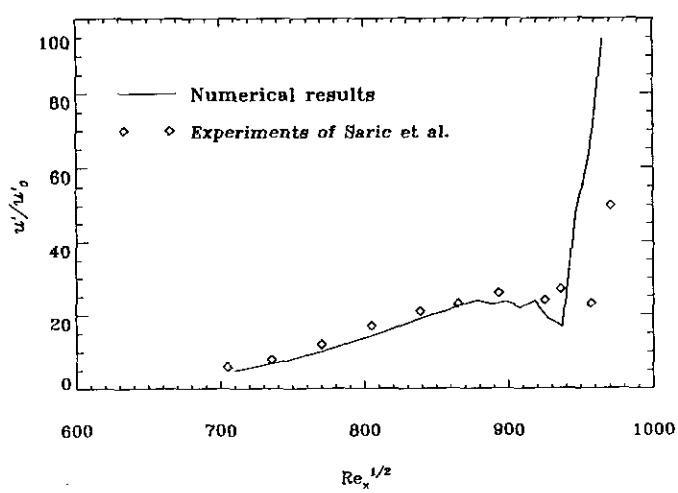

FIG. 20. Comparison of normalized perturbation velocity amplitude obtained at $u = 0.4$ as a function of Re_δ with experimental results of Saric *et al.* [17].

There is really a lack of reliable experimental data for transitional flow that can be used to judge the computational results. Also, we need finer grids to obtain better resolution for poston-set flow. Thus, at those coarse grid levels, we must sacrifice small eddy resolution. Nevertheless, the results apparently show physically correct simulation for the whole process of flow transition.

The running time of the code is around 22 μs/grid-point/time-step (equivalent to 5 μs/grid-point/iteration) on a single YMP CPU, and the memory requirement is 34 words/grid-point.

8. CONCLUDING REMARKS

- Fully implicit time-marching and fourth-order finite difference schemes on stretched and staggered grids provide enough accuracy to simulate preonset transitional flow on a relatively coarse grid. Computational results agree with linear stability theory, secondary instability theory, and some experiments.
- Approximate line-box relaxation with semi-coarsening multigrid is very efficient for solving 3D Navier–Stokes equations.
- Fine–coarse–fine grid dissipation techniques successfully maintain the spatial DNS code simulation of the whole process of transition before and after laminar flow breakdown. The current spatial DNS code is able to reproduce the whole process of K-type and C-type transition observed by Klebanoff *et al.* [18] and Kachanov *et al.* [19].
- Simulation with relatively coarse grids can still provide qualitatively correct prediction for transitional flow. It shows that the large eddies play the dominant role in the process of flow transition.

ACKNOWLEDGMENTS

The authors thank NASA Langley Research Center and NASA Lewis Research Center for the sponsorship. The authors also appreciate the very helpful discussions with Drs. T. H. Shih, Z. G. Yang, and A. Shabbir at ICOMP/NASA Lewis Research Center. The authors are grateful to Dr. S. McCormick for his help.

REFERENCES

1. S. A. Orszag and L. C. Kells, *J. Fluid Mech.* **96,** 159 (1980).
2. A. Wray and M. Y. Hussaini, *Proc. R. Soc. London A* **392,** 373 (1984).
3. L. Kleiser and E. Laurien, AIAA Paper No. 85-0566, 1985 (unpublished).
4. T. A. Zang and M. Y. Hussaini, *Appl. Math. Comput.* **19,** 359 (1986).
5. T. A. Zang, S. E. Krist, G. Erlebacher, and M. Y. Hussaini, AIAA Paper No. 87-1204, 1987 (unpublished).
6. H. Fasel, *J. Fluid Mech.* **78,** 355 (1976).
7. H. Fasel and H. Bestek, "Investigation of Nonlinear, Spatial Disturbance Amplification on Plane Poiseuille Flow," in *Laminar-Turbulent Transition,* edited by R. Eppler and H. Fasel, (Springer-Verlag, Germany, 1980), p. 173.
8. P. R. Spalart, "Direct Numerical Study of Leading-Edge Contamination," in *Fluid Dynamics of Three-Dimensional Turbulent Shear Flows and Transition,* AGARD-CP-438, 5.1–5.13, 1989.
9. H. Fasel and U. Konzelmann, *J. Fluid Mech.* **221,** 311 (1990).
10. G. Danabasoglu, S. Biringen, and C. L. Streett, AIAA Paper No. 91-0234, 1991 (unpublished).
11. R. Joslin, C. Streett, and C. Chang, NASA TP-3205, 1992 (unpublished).
12. L. Kleiser and T. A. Zang, *Annu. Rev. Fluid Mech.* **23,** 495 (1991).
13. Z. Liu and C. Liu, *J. Comput. Wind. Eng.* **52,** 412 (1992).
14. C. Liu and Z. Liu, *J. Comput. Phys.* **106,** 92 (1993).
15. Z. Liu, Ph.D. thesis, University of Colorado at Denver, 1993.
16. K. L. Suder, J. E. O'Brien, and E. Reshotko, NASA TM-100913, 1988 (unpublished).
17. W. S. Saric, V. V. Kozlov, and C. Ya. Levchenko, AIAA Paper No. 84-0007, 1984 (unpublished).
18. P. S. Klebanoff, K. D. Tidstrom, and Sargent, *J. Fluid Mech.* **12,** 1 (1962).
19. Y. S. Kachanov, V. V. Kozlov, and V. Y. Levchenko, *Fluid Dynamics* **12,** 383 (1978).